On MRI turbulence quantification[☆]

Petter Dyverfeldt[a,b,c,*], Roland Gårdhagen[b,c], Andreas Sigfridsson[a,c,d],
Matts Karlsson[b,c], Tino Ebbers[a,b,c]

[a]Division of Cardiovascular Medicine, Department of Medical and Health Sciences, Linköping University, Linköping, Sweden
[b]Division of Applied Thermodynamics and Fluid Mechanics, Department of Management and Engineering, Linköping University, Linköping, Sweden
[c]Center for Medical Image Science and Visualization (CMIV), Linköping University, Linköping, Sweden
[d]Division of Medical Informatics, Department of Biomedical Engineering, Linköping University, Linköping, Sweden

Abstract

Turbulent flow, characterized by velocity fluctuations, accompanies many forms of cardiovascular disease and may contribute to their progression and hemodynamic consequences. Several studies have investigated the effects of turbulence on the magnetic resonance imaging (MRI) signal. Quantitative MRI turbulence measurements have recently been shown to have great potential for application both in human cardiovascular flow and in engineering flow. In this article, potential pitfalls and sources of error in MRI turbulence measurements are theoretically and numerically investigated. Data acquisition strategies suitable for turbulence quantification are outlined. The results show that the sensitivity of MRI turbulence measurements to intravoxel mean velocity variations is negligible, but that noise may degrade the estimates if the turbulence encoding parameter is set improperly. Different approaches for utilizing a given amount of scan time were shown to influence the dynamic range and the uncertainty in the turbulence estimates due to noise. The findings reported in this work may be valuable for both in vitro and in vivo studies employing MRI methods for turbulence quantification.
© 2009 Elsevier Inc. All rights reserved.

Keywords: Turbulence quantification; Turbulent flow; Phase-contrast magnetic resonance imaging; Constriction; Numerical flow phantom

1. Introduction

While normal cardiovascular flow is predominantly laminar, turbulent flow accompanies many forms of cardiovascular disease. In the human arterial tree, turbulence causes pressure drops over stenoses and may increase the risk for hemolysis [1] as well as platelet activation and thrombus formation [2,3]. Additionally, ample evidence suggests that turbulence is involved in the pathogenesis of atherosclerosis [4–6]. With a growing awareness of the implications of abnormal hemodynamics, the demand for reliable tools for the quantitative assessment of blood flow disturbances is increasing [7].

Turbulent fluid motion can be described as "an irregular condition of flow in which the various quantities show a random variation with time and space coordinates, so that statistically distinct average values can be discerned" [8]. By employing ensemble, time or space averaging, a velocity component u can be statistically separated into the averaged mean velocity U and the fluctuating velocity u' according to $u=U+u'$ [9]. The intensity of the velocity fluctuations can be quantified by the standard deviation $\sigma = \text{sqrt}\left(\overline{u'^2}\right)$ (m/s). Under the ergodic hypothesis, ensemble, time and space averages are interchangeable [10]. This means for example that sampling over a spatial area that encompasses all turbulence space scales yields the same result as a convergent value sampled over time.

Several studies have investigated the effects of turbulent flow on the magnetic resonance imaging (MRI) signal in order to establish methods for quantifying turbulence [11–18]. Recently, an in vitro study indicated good agreement between the turbulence quantities obtained by MRI and particle image velocimetry [19]. In addition, MR turbulence quantification was recently successfully applied in vivo for the first time [20]. Prior to this, MR methods for

---

  * Corresponding author. Division of Cardiovascular Medicine, Department of Medical and Health Sciences, Linköping University, SE-581 83 Linköping, Sweden.
  E-mail address: petter.dyverfeldt@liu.se (P. Dyverfeldt).

the quantification of turbulence have been sparingly applied [21]. This may partly be attributed to earlier limitations in scanner hardware; the advantages offered by modern MRI scanners, such as increased signal-to-noise ratio through the use of improved receiver coils and reduction of echo time through the use of high-performance gradients can be expected to increase their utilization. Moreover, usability may be enhanced by clarifying specific aspects of MR turbulence measurements that facilitate adequate application of the technique. Here, we will examine the practical consequences of some of the assumptions which underlie MR quantification of turbulence and investigate how intravoxel mean velocity variations and noise affect the turbulence estimates. All methods that utilize the MR signal magnitude for turbulence quantification are subjected to the same sources of error; however, different approaches for obtaining turbulence estimates may be differently affected.

The objective of this work was to investigate potential pitfalls and sources of error in MR measurements of turbulence quantities and to outline strategies for minimizing their effects. This was done by means of theoretical derivations and numerical simulations.

2. Theory

MRI flow quantification of the mean velocity, U, is a standard clinical tool and a powerful research tool that can be used to quantify different components of blood transiting the left ventricle [22], for example. The most common MR tool for quantification of flow is phase-contrast (PC) MRI [23] where bipolar gradients are used to apply flow sensitivity. Spins moving under the influence of a bipolar gradient accumulate phase according to

$$\varphi = \gamma \int_0^{2\tau} G(t)x(t)\mathrm{d}t, \tag{1}$$

where γ is the gyromagnetic ratio, τ is the duration of half the bipolar gradient and $G(t)$ describes the gradient wave-form. In PC-MRI, spins are assumed to move with a constant velocity and Eq. (1) can be written as $\varphi = uk_v$, where $k_v = \gamma \int_0^{2\tau} G(t)t\mathrm{d}t$ describes the amount of applied flow sensitivity. The phase difference between two, or more, flow encoding segments acquired with different k_v values is proportional to the fluid velocity. The net phase of all the spins within a voxel provides the mean velocity U [24]. For a voxel centered at a given spatial position, the complex-valued PC-MRI signal can be described by [25]

$$S(k_v) = C \int_{-\infty}^{\infty} s(u)\mathrm{e}^{-ik_vu}\mathrm{d}u, \tag{2}$$

where C is a constant influenced by relaxation parameters spin density and receiver gain; u is the velocity; and $s(u)$ is the spin velocity distribution within the voxel.

In contrast to MRI measurements of the mean velocity, where the phase of the complex-valued MR signal contains the information of interest, quantification of the fluctuating velocity, u', can be achieved by exploiting the effects of turbulence on the MR signal magnitude. With Eq. (1) as a starting point, Gao and Gore [14] presented a theoretical analysis of the relation between turbulent flow and the MR signal. They found the effects of turbulence to be dependent on the Lagrangian integral time scale, T_0, which is a measure of the evolution time of turbulence. For an ideal bipolar gradient, their expression describing the dependence of T_0 appears as

$$|S(k_v)| = |S(0)|\mathrm{e}^{-\sigma_{GG}^2 k_v^2 T_0 \tau^{-1}\left(2/3 - 2T_0^2/\tau^2 + T_0^3/\tau^3(3 - 4\exp(-\tau/T_0) + \exp(-2\tau/T_0))\right)}, \tag{3}$$

where σ_{GG} represents the ensemble averaged standard deviation [14]. Gao and Gore [14] noticed that special cases emerged when T_0 is long or short in relation to τ. Their simplification for long time scales appears as

$$|S(k_v)| = |S(0)|\mathrm{e}^{-(1/2)\sigma^2 k_v^2}. \tag{4}$$

In the Gao and Gore [14] theory, it is assumed that $\ln(|S|/|S_0|)$ is directly proportional to k_v^2. This is equivalent to assuming that $|S(k_v)|$ has a Gaussian distribution. Gao and Gore [14] prescribed measurements with several k_v values to find the expected linear relationship between $\ln(|S|/|S_0|)$ and k_v^2 and, thereby, σ. The work of Gao and Gore [14], in combination with others [15,16], constitutes a theoretical and experimental foundation for the effect of turbulent time scales on the MR signal. The method of Gao and Gore [14] and the work of their predecessors have been reviewed by Kuethe and Gao [16].

Following a different theoretical approach which origi-nated from Eq. (2), Dyverfeldt et al. [18] derived a relation which is similar to Eq. (4) and noticed that the data required for turbulence quantification can be obtained from a standard PC-MRI measurement. The theory underlying this method exploits the fact that the spin velocities within a voxel can be assumed to be normally distributed in turbulent flow. As a result, $s(u)$ can be expressed as the Gaussian probability density function and Eq. (2) can be written as

$$S(k_v) = C\mathrm{e}^{-(1/2)\sigma^2 k_v^2 - iUk_v}. \tag{5}$$

In Eq. (5), σ represents the intravoxel spin velocity standard deviation (IVSD) which, under the assumption of ergodicity, equals the ensemble averaged standard deviation. Since Eq. (2) is a Fourier transform, $|S(k_v)|$ is Gaussian distributed also in the theory underlying this method. By combining two MRI signals acquired with different k_v values, $S(k_{v_1})$ and $S(k_{v_2})$, the quantification of the velocity fluctuations can be obtained directly from the signal magnitude relationship according to $\sigma = \mathrm{sqrt}[2\ln(|S(k_{v_2})|/|S(k_{v_1})|)/(k_{v_1}^2 - k_{v_2}^2)]$, $|k_{v_1}| \neq |k_{v_2}|$. This approach will be referred to here as IVSD mapping and σ values obtained in this manner will be abbreviated σ_{IVSD}. In

practice, it is convenient to set one of the k_v values in the preceding equation to 0 so that

$$\sigma_{IVSD} = \mathrm{sqrt}\left[\frac{2}{k_v^2}\ln(|S(0)|/|S(k_v)|)\right]. \tag{6}$$

This results in a direct relationship between the nonzero k_v and the velocity encoding range (VENC) of the corresponding PC-MRI acquisition: VENC=π/k_v. In PC-MRI velocity mapping, the VENC defines a strict dynamic range and velocities outside the VENC are aliased. In IVSD mapping, the VENC defines the IVSD value which is resolved with best sensitivity, $\tilde{\sigma}$, according to $\tilde{\sigma}$=VENC/π. This optimum is achieved at a signal magnitude ratio $|S|/|S_0|$ of approximately 0.6 (analytically: $e^{-1/2}$) [18].

The resemblance between Eq. (4) and Eq. (5) reflects the fact that, by originating from Eq. (2), the IVSD derivation implicitly requires that $\tau \ll T_0$. Experimental MRI methods capable of providing data for the calculation of T_0 [15,26] have been described but would have limited applicability in vivo. However, as suggested by Gao and Gore [14], T_0 can be estimated by l/σ, where l, the characteristic length, is approximately one third of the vessel diameter. Recently, IVSD mapping was carried out in a range of human cardiovascular applications and the highest values of σ, found in poststenotic aortic flow, were about 0.7 m/s [20]. This gives a worst-case T_0 estimate of about 10 ms and thus, for in vivo investigations at modern clinical MRI scanners where the duration of one bipolar gradient lobe is typically around 0.5 ms, the short time scale assumption seems valid and preferable.

3. Materials and methods

An important assumption underlying MR turbulence methods is that $|S(k_v)|$ has a Gaussian distribution, even though other distributions may be used as well [18]. Also, MR methods for turbulence quantification require that the voxels are sampled in a way which sufficiently encompasses the turbulence scales. The conditions for this to hold are dependent on the nature of the flow in combination with imaging parameters. Intravoxel mean velocity variations will

contribute to the distribution of $s(u)$ and noise will directly affect the appearance of $|S(k_v)|$; in this study, the effects of these inevitable sources of error are investigated. Additionally, the effects of noise on different approaches for obtaining the standard deviation of $|S(k_v)|$ are compared. In exploring these aspects of MR turbulence measurements, we utilize the theory underlying IVSD mapping [18] in combination with a numerical flow phantom and two different MR simulation approaches. The MR simulations are tailor made to allow investigations of the specific questions of interest.

3.1. Numerical flow phantom

A numerical flow phantom consisting of time-resolved data of steady turbulent flow in a 14.6-mm-diameter straight pipe with a 75% area reduction cosine-shaped stenosis (Fig. 1A) was generated from large eddy simulations (LES) [27]; Newtonian flow with Reynolds number of 2000 at the inlet was considered. At the inlet, the flow had a fully developed laminar profile with superimposed velocity disturbances. Inlet and outlet were placed at four unconstricted pipe diameters upstream and 21 diameters downstream from the center of the stenosis, respectively.

LES is a computational technique in which the larger turbulent scales are resolved, while the smaller ones are modeled, and instantaneous velocity fields separated by small, finite, time steps are computed. The approach used here has previously been validated against direct numerical simulations and laser Doppler anemometry [28]. A structured mesh consisting of 6.2 million cells was constructed in ANSYS Gambit 2.3 (ANSYS, Pittsburgh, PA, USA), and all computations were performed with ANSYS Fluent 6.3 (ANSYS) on the Linux cluster Neolith (National Supercomputer Centre, Linköping, Sweden). The solution was advanced with a time step of 50 µs. Converged values of σ taken over time, σ_{time} (requiring at least 10,000 time steps), were acquired along the centerline of the numerical flow field.

3.2. Gaussian distributions and scales of turbulence

In turbulent flow, eddies exist on a wide range of time and space scales. Accurate values of σ can only be
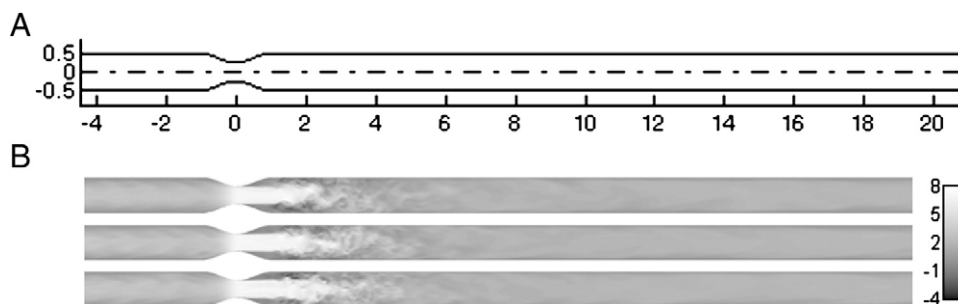

Fig. 1. (A) Schematic of the numerical flow phantom used in this work. (B) Images of the instantaneous axial velocity in the numerical flow phantom at three different time points. The axes show the distance from the center of the stenosis, normalized by the unconstricted pipe diameter. The main flow direction is from left to right in the image.

obtained by sampling the velocity field in a way that sufficiently encompasses the turbulence scales [29]. In experimental assessment of turbulence, sampling can be done over space and/or time. In laser Doppler anemometry, for example, repeated measurements of the velocity at a single point are carried out over a sufficiently long period of time. MR image voxels are built up by samples taken over both space and time, and, therefore, the turbulence scales are sampled in both the temporal and the spatial domain. The contribution from the spatial domain is simply determined by the voxel size. How well the temporal dimension helps in building up a voxel suitable for turbulence quantification is dependent on the time separation between each sample.

Simulations of MR turbulence measurements were carried out on the numerical flow phantom by considering isotropic voxels of $2 \times 2 \times 2$ mm^3 along the centerline of the phantom. To reflect the effect of the time separation between the acquisitions of two consecutive phase-encoding lines on the sampling of the turbulence scales, each voxel comprised data from 20 time steps in the numerical flow phantom, separated by 20 ms. This corresponds to the time difference between two phase-encoding lines in an interleaved three-directional PC-MRI experiment with a TR of 5 ms.

The intravoxel velocity distribution, $s(u)$, was obtained by computing a probability density estimate of the spin velocities within each voxel. Only the velocity component in the main flow direction was studied. From $s(u)$, $S(k_v)$ was computed by means of Eq. (2) with k_v set to match the highest σ values in the numerical flow phantom. Finally, σ_{IVSD} was computed according to Eq. (6). The values of σ_{IVSD} were compared with σ_{time}, obtained as described above, and σ_{rms}, which was computed directly from the velocities within each voxel as the root-mean-square deviation from their mean. Note that, by definition, σ values obtained by MR turbulence measurements are estimations of σ_{rms}.

Furthermore, $S(k_v)$ was sampled by computing Eq. (2) for a range of k_v values. The distributions of $s(u)$ and $|S(k_v)|$ obtained in this manner were compared to Gaussian curves, using the standard deviation that was obtained by the simulated IVSD measurements.

3.3. Intravoxel mean velocity variations

Variations in the mean velocity within a voxel will contribute to the intravoxel distribution of spin velocities and thereby alter the appearance of $S(k_v)$. Denoting the intravoxel velocity distribution caused by mean velocity variations alone as $s_{MVV}(u)$ and the distribution attributable to turbulence as $s_{turb}(u)$, the joint intravoxel velocity distribution can be obtained by convolution:

$$s(u) = s_{MVV}(u) * s_{turb}(u), \qquad (7)$$

The Fourier transform relationship in Eq. (2) implies that Eq. (7) can be written as

$$S(k_v) = S_{MVV}(k_v) S_{turb}(k_v), \qquad (8)$$

where $S(k_v)$ is the signal obtained from the measurement. Rearranging and inserting Eq. (8) into Eq. (6) gives:

$$\sigma_{turb} = \mathrm{sqrt}\left[\sigma_{IVSD}^2 - \frac{2}{k_v^2} \ln\left(\frac{|S_{MVV}(0)|}{|S_{MVV}(k_v)|} \right) \right]. \qquad (9)$$

Based on the measured σ value and an estimation of the intravoxel mean velocity variation, Eq. (9) thus provides a way of estimating and compensating for the effects of intravoxel mean velocity variations on MR turbulence measurements. As seen from Eq. (9), the effect decreases with increasing turbulence.

In this work, the effects of intravoxel mean velocity variations were addressed by studying the spatial acceleration along the centerline of the numerical flow phantom. The acceleration was approximated as the linear velocity gradient over a voxel. In this way, pure spatial acceleration results in a boxcar (uniform) spin velocity distribution within the voxel. The quotient $|S_{MVV}(k_v)|/|S_{MVV}(0)|$ in Eq. (9) can then be derived from Eq. (2) and appears as $|\mathrm{sinc}(ak_v/2)|$, where a is the velocity difference over the voxel.

3.4. Noise and dynamic range

It has previously been noticed that MR turbulence measurements will provide unreliable estimates when the difference in signal magnitude between S and S_0 is in the same order of magnitude as the noise [16]. However, due to the Rician distribution of MR magnitude data, noise does not only affect the precision of MR turbulence measurements but may also cause bias. Since the best sensitivity in IVSD mapping is obtained by using a k_v value of $1/\tilde{\sigma}$, where $\tilde{\sigma}$ is the σ value of interest, the dynamic range can suitably be described in terms of $\tilde{\sigma}$. σ values much lower than $\tilde{\sigma}$ cause a poor difference in signal magnitude between S and S_0. Due to noise, estimates of low σ values are consequently resolved with lower accuracy. This is not of great concern, however, since σ values much lower than the value of interest are presumably of limited clinical significance. More importantly, σ values considerably greater than $\tilde{\sigma}$ will result in almost zero true signal magnitude in $S(k_v)$. Since the
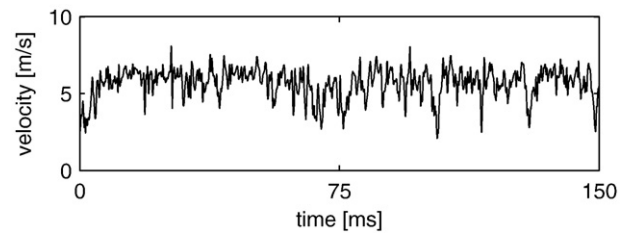

Fig. 2. Plot of the axial velocity component over time in the numerical flow phantom at 2.5 diameters downstream from the stenosis.
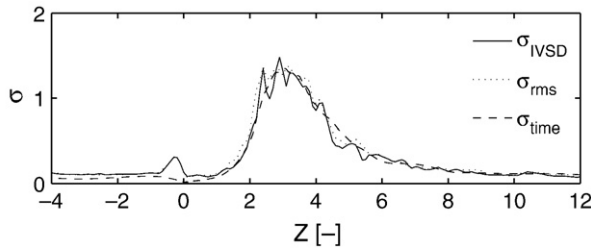
Fig. 3. Turbulence intensity in the axial direction along the centerline of the numerical flow phantom. Solid line: σ_{IVSD} as obtained by a simulated MR turbulence measurement. Dotted line: True standard deviation of the velocities within each voxel. Dashed line: Convergent values of the standard deviation as sampled over time in the numerical phantom. Z shows the distance from the center of the stenosis, normalized by the unconstricted pipe diameter ($Z=1 \Leftrightarrow 14.6$ mm). The main flow direction is the positive Z-direction.

modulus of $S(k_v)$ is used, the effective noise will, in these cases, have a nonzero mean value, implying that the reconstructed signal magnitude will be overestimated and, consequently, that σ will be underestimated. To what extent this occurs is determined by the signal-to-noise ratio (SNR) and the k_v value. As the true signal in these cases is close to 0, the reconstructed signal magnitude can be considered to be constituted by noise alone. A useful expression for estimating the effect of noise in MR turbulence mapping can thus be obtained simply by letting the flow-sensitized

signal $S(k_v)$ be the mean amplitude of the noise, n_m. In this way, Eq. (6) can be written as

$$\hat{\sigma} = \frac{1}{k_v} \text{sqrt}[2\ln(|S_0|/n_m)], \tag{10}$$

which allows for an estimation of the σ value at which the true signal magnitude equals the mean magnitude of the noise. At σ values greater than $\hat{\sigma}$, noise will, on average, dominate the measured signal, implying an underestimation of σ. A corresponding approach for diffusion-weighted imaging has been presented by Jones and Basser [30].

The impact of noise on MR turbulence measurements was assessed by using a simulation approach in which noise was added to a theoretically ideal MR signal. This simulation did not comprise the numerical flow phantom used above. Instead, to exclude the effects of the flow condition and solely focus on the effects of noise, a complex-valued theoretical MR signal $S_{\text{theory}}(k_v \cdot \sigma_{\text{true}})$ was generated by inserting a range of $k_v \cdot \sigma_{\text{true}}$ values into Eq. (5). σ_{true} represents a true intravoxel velocity standard deviation. The multiplication of k_v and σ_{true} allows for findings to be expressed in more general terms. The maximum value of S_{theory} was 1 for $k_v \cdot \sigma_{\text{true}}=0$. Simulation of a measured signal, $S_{\text{measured}}(k_v \cdot \sigma_{\text{true}})$, was carried out by adding Gaussian distributed noise with zero mean and variance of 0.0025 to the real and the imaginary part of the theoretical signal,
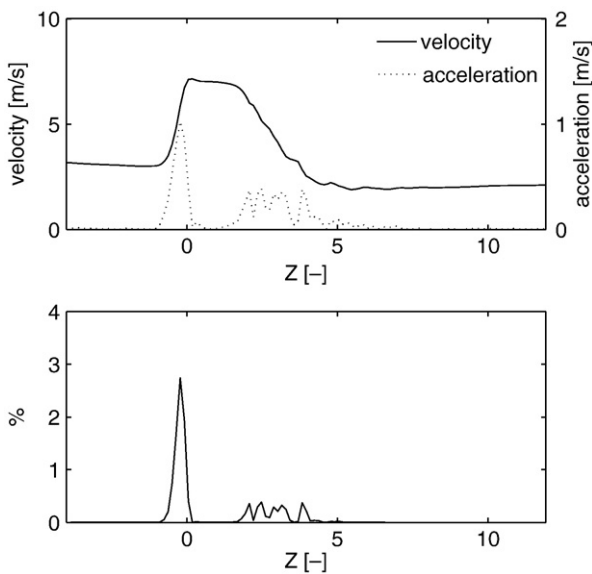

Fig. 4. The effects of spatial acceleration along the centerline of the numeric flow phantom. Upper panel: The mean velocity along the centerline of the numerical flow phantom (solid line, left vertical axis) is plotted together with the amplitude of the spatial acceleration (dotted line, right vertical axis). Lower panel: Relative to the k_v value used in the MR simulation, the contribution from spatial acceleration to the measured IVSD values is less than 3%. Z shows the distance from the center of the stenosis, normalized by the unconstricted pipe diameter ($Z=1 \Leftrightarrow 14.6$ mm). The main flow direction is the positive Z-direction.
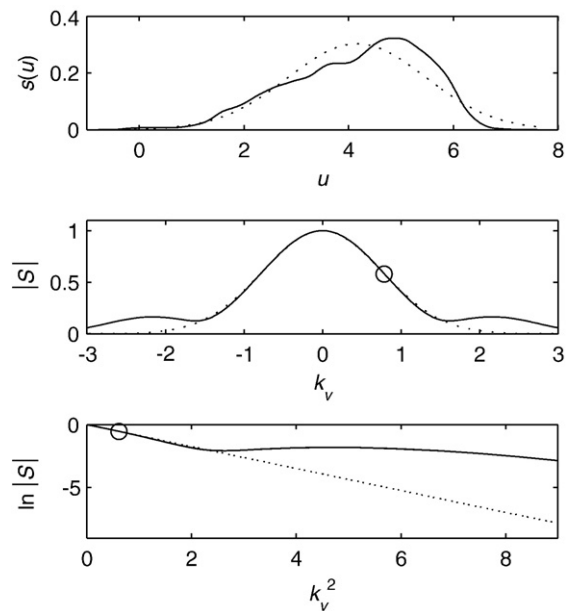

Fig. 5. Upper panel: The appearance of the intravoxel spin velocity distribution $s(u)$ (solid line) at the centerline position $Z=3$ is compared to a Gaussian curve (dotted line) with the standard deviation obtained in the simulated MR turbulence measurement. Middle panel: $|S(k_v)|$ (solid) and a corresponding Gaussian curve (dotted). Lower panel: $\ln(S(k_v^2))$. The circles indicate the k_v value used in the simulation. Note, in the lower panels, that the two curves deviate only at k_v values clearly higher than those used in the simulation.

thus giving it a maximum SNR of 20 for $k_v \cdot \sigma_{true}=0$, and decreasing SNR with increasing values of $k_v \cdot \sigma_{true}$. $|S_{measured}(k_v \cdot \sigma_{true})|$ is thus Rician distributed and represents the MR signal magnitude that would have been measured at the present SNR. From $|S_{measured}(k_v \cdot \sigma_{true})|$, $\hat{\sigma}$ was computed by means of Eq. (10). Estimates of σ_{IVSD} were thereafter obtained using Eq. (6) and then multiplied with k_v to yield $k_v \cdot \sigma_{IVSD}$. The resulting values of $k_v \cdot \sigma_{IVSD}$ thus differed from $k_v \cdot \sigma_{true}$ only due to noise. This computation was repeated 100,000 times so that mean and standard deviation values of $S_{measured}$ and $k_v \cdot \sigma_{IVSD}$ could be obtained for each value of $k_v \cdot \sigma_{true}$. The standard deviation of $S_{measured}$ and $k_v \cdot \sigma_{IVSD}$ represents uncertainty due to noise.

When additional scan time is available, different approaches for obtaining σ can be used; the effect of noise on the dynamic range will depend on the approach which has been chosen. Here, three different approaches were evaluated. The IVSD method without additional signal averaging was included as a reference and contrasted to three approaches that require a twofold increase in scan time:

namely, IVSD mapping with three averages of $S(k_v \cdot \sigma_{true}=1)$, standard linear least-squares fit of four measurements of $\ln(|S[(k_v \cdot \sigma_{true})^2]|)$ and weighted linear least-squares fit of four measurements of $\ln(|S[(k_v \cdot \sigma_{true})^2]|)$. $k_v \cdot \sigma_{true}$ values of 0, 0.6, 1 and 1.4 were used in the least-squares approaches. Knowing that $|S|/|S_0|=0.6$ provides the best accuracy and that excessively higher and lower signal ratios are disadvantageous, we hypothesize that a weighted least-squares fit is advantageous, if compared to an unweighted fit. In the present study, the weights were empirically set according to a Gaussian filter with standard deviation of 0.2, centered at $|S|/|S_0|=0.6$.

4. Results

Maps of the instantaneous axial velocity in a center-plane of the numerical flow phantom at three different time points (Fig. 1B) indicate that the largest temporal velocity variations are present around $Z=3$. The velocity
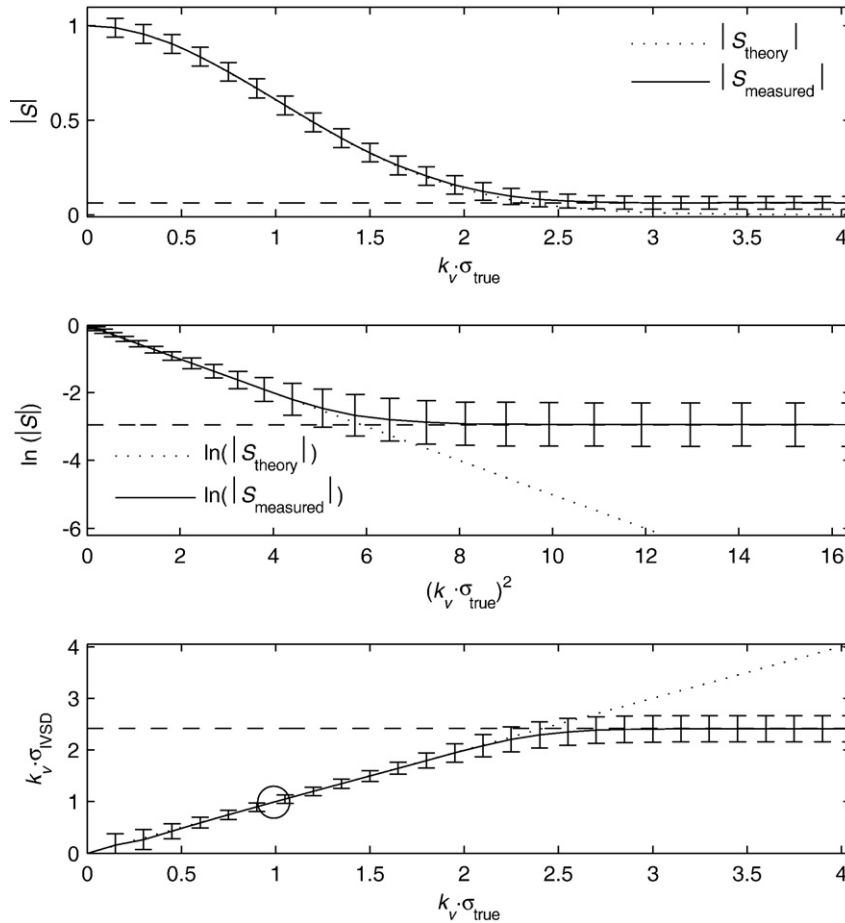

Fig. 6. Dynamic range in PC-MRI IVSD mapping at SNR ≤20. The solid lines show the mean of 100,000 estimates, and the error bars represent ±1 S.D. The dotted lines show the theoretical appearance in the absence of noise. Upper panel: Compared to the theoretical signal behavior ($|S_{theory}(k_v \sigma_{true})|$), the measured signal ($|S_{measured}(k_v \sigma_{true})|$) is overestimated at low SNR. The dashed line shows the lowest value of $|S|$ that can be measured without, on average, being overestimated. Middle panel: Corresponding plots for $\ln(|S(k_v \sigma_{true})^2|)$. Lower panel: Measured IVSD value vs. true intravoxel velocity standard deviation compared to the theoretical relation. The dashed line shows the maximum value of $k_v \sigma_{IVSD}$ that can be measured without being underestimated at the present SNR, computed according to Eq. (10). The circle indicates the IVSD value with lowest uncertainty.

over time at the centerline position $Z=2.5$ is plotted in Fig. 2.

A comparison between a simulated MR turbulence measurement (σ_{IVSD}), the root-mean-square deviation of the intravoxel velocities from their mean, σ_{rms}, and σ_{time} as obtained by sampling the numerical flow field over time is shown in Fig. 3.

The amplitude of the spatial acceleration along the centerline of the numerical flow phantom is shown in the upper panel of Fig. 4 along with the mean velocity. The lower panel shows the contributions from spatial acceleration, relative to the k_v value used in the simulated measurement. The greatest effect is seen at the site of flow acceleration in the stenosis where turbulence is low. In the area of elevated turbulence around $Z=3$, the effect is less than 1%.

Fig. 5 shows the appearance of the intravoxel spin velocity distribution $s(u)$ and its Fourier equivalent $|S(k_v)|$ at $Z=3$. Additionally, the appearance of $\ln(|S(k_v^2)|)$ is shown. The circles indicate the k_v value used in the simulation. Note that, although the agreement between $s(u)$ and the Gaussian curve appears poor, $|S(k_v)|$ deviates from the Gaussian curve mainly at values clearly above the used k_v.

Fig. 6 outlines the appearance of the dynamic range in MR turbulence measurements. As compared to $|S_{theory}(k_v \cdot \sigma_{true})|$, $|S_{measured}(k_v \cdot \sigma_{true})|$ is on average overestimated at low SNR. The error bars show the uncertainty in the estimates of $S_{measured}$ due to noise (bar height=±1 S.D.). Corresponding plots for $\ln(|S(k_v \cdot \sigma_{true})^2|)$ can be seen in the middle panel. In the lower panel, values of σ_{IVSD}, normalized by multiplication with k_v, are plotted against $k_v \cdot \sigma_{true}$ (solid line) with error bars showing the uncertainty of the IVSD estimates due to noise (bar height=±1 S.D.). The dashed line shows the maximum value, $k_v \hat{\sigma}$, that can be measured without being underestimated at the present SNR. Additionally, the circle indicates the IVSD value with lowest uncertainty, $\tilde{\sigma}$.

A comparison between different approaches for utilizing additional scan time and their effects on the dynamic range can be seen in Fig. 7B–D. The IVSD method without additional signal averaging is included as a reference (Fig. 7A). In each panel, the quantity which has been measured is plotted against true intravoxel velocity standard deviation, σ_{true}, normalized by multiplication with k_v (solid lines), with error bars showing the uncertainty due to noise. The dotted lines show the
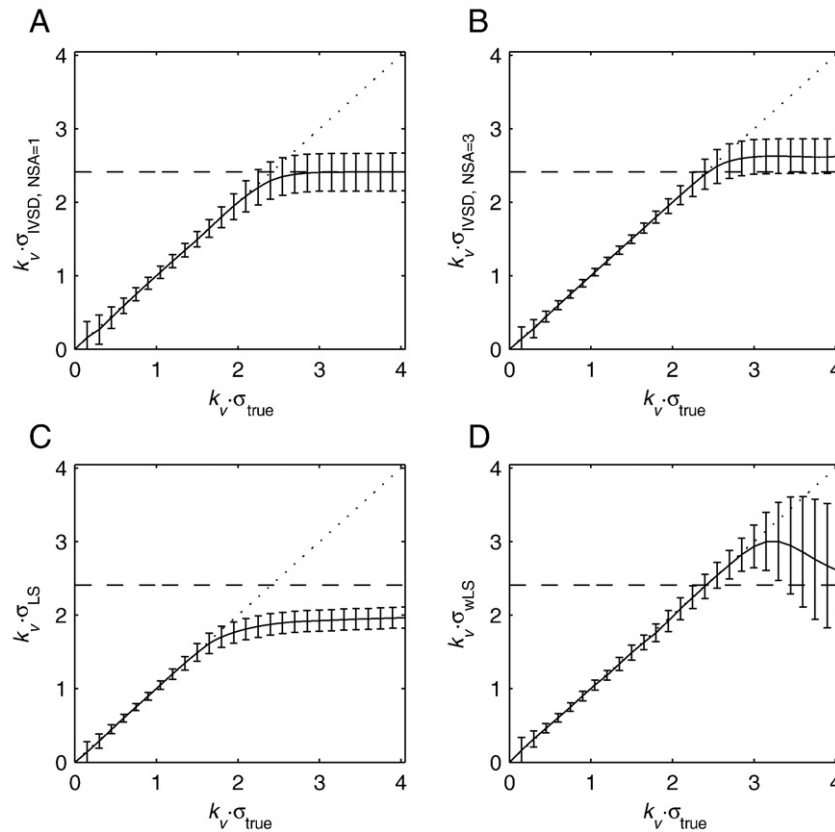

Fig. 7. Comparison between different approaches for utilizing additional scan time and their effects on the dynamic range. In each panel, the average of 100,000 estimates is plotted against true intravoxel velocity standard deviation, σ_{true}, normalized by multiplication with k_v (solid lines), with error bars showing ±1 S.D. The dotted lines show the ideal theoretical relations. The dashed lines show the maximum values that can be measured without, on average, being underestimated when using IVSD mapping without additional signal averaging. (A) The IVSD method without additional signal averaging is included as a reference. (B) The IVSD method with three signal averages of $S(k_v)$. (C) Standard least-squares (LS) fit using four k_v values. (D) Weighted least-squares (wLS) fit using four k_v values. NSA=Number of signal averages.

theoretical relation and the dashed lines show $\hat{\sigma}$ for IVSD mapping without additional signal averaging. Note that IVSD mapping with signal averaging of $S(k_v)$ (Fig. 7B) and the proposed weighted least-squares approach (Fig. 7D) extends the dynamic range, whereas the standard least-squares approach has the opposite effect (Fig. 7C).

5. Discussion

In this study, fundamental aspects of the theory underlying MR turbulence measurements have been investigated. Methods for assessing the effects of noise and intravoxel mean velocity variations have been derived. By means of two different simulation approaches, the consequences of these sources of error on the MR signal used for turbulence quantification have been demonstrated.

In theory, MR methods for the quantification of turbulence seek to estimate σ_{rms}, the root-mean-square deviation of the intravoxel velocities from their mean. When the flow is ergodic and the voxels are built up by samples that sufficiently reflect the turbulence scales, the turbulence quantity measured by MRI will correspond to a σ value measured by, for example, laser Doppler anemometry, given that this method too is applied with a sufficient sampling of the turbulence scales. A comparison between σ_{IVSD} as obtained by a simulated MR measurement and σ_{rms} showed excellent agreement (Fig. 3) and demonstrates the potential of MR turbulence quantification. Additionally, σ_{IVSD} agreed well with σ_{time}, which was obtained by sampling the numerical flow phantom over time. Notwithstanding the MR simulation approach used here, these findings support the results recently reported by Elkins et al. [19] which indicated a good agreement between turbulence quantities obtained by MRI and particle image velocimetry.

It should be noted that this study did not comprise measurements. Instead, to allow a thorough investigation of specific aspects of the theory underlying MR turbulence quantification, tailor-made MR simulations were designed. Performing a complete MR simulation of turbulent flow was beyond the scope of this study and remains a challenge. However, since the gradient waveform is reduced to one variable, k_v, and relaxation parameters have no effect on the validity of the MR methods for quantification of turbulence used in this study, direct computations on a numerical flow phantom provide a good way of examining specific aspects of the accuracy of these methods. The numerical flow phantom used in this work allowed us to synthesize the MR signal directly from the intravoxel velocity distribution, using Eq. (2), and thereby simulate MR turbulence measurements. The flow in the numerical phantom is visualized in Fig. 1 for three time points. The plot of instantaneous velocity at the centerline position Z=2.5 (Fig. 2) shows the apparently random behavior which is characteristic for turbulent flow. Although 6.2 million cells were used in the mesh, the voxels in the area of high turbulence encompassed only about 2000 cells. Combining data from multiple time steps in the numerical flow phantom thus helped in increasing the apparent intravoxel spin density. Still, the relatively low number of cells within the 2^3-mm^3 voxels may have affected the statistical analysis of the intravoxel velocities and thereby the appearance of $s(u)$ and $S(k_v)$ in the MR simulations.

Approaches for acquiring data suitable for turbulence quantification can be described with respect to the importance of sampling the turbulence scales. By definition, when $\tau \ll T_0$, the turbulent eddies appear stationary over the short duration of the observation time. The voxel size used in an experiment is often smaller than the largest turbulence space scales which can be of the same order of magnitude as the vessel, or pipe, diameter. This has important implications for the design of pulse sequences for measuring turbulence quantities and implies that sampling the voxel at several points in time may be necessary for sufficient inclusion of the turbulence scales. In MR imaging, the temporal dimension comes into play in different ways and how well it helps in building up a voxel suitable for turbulence quantification may depend on factors such as the choice of gradient encoding scheme, the k-space trajectory and the number of signal averages. The Lagrangian time scale, T_0, is an order of magnitude representation of the statistical memory of the flow and it may therefore be preferable to sample the temporal dimension with a time difference of more than T_0 between each sample. For in vivo applications where cardiac-gated time-resolved PC-MRI is most often used, two consecutive phase-encoding lines are temporally separated by the duration of one cardiac cycle, and this is not an issue. If a multiple number of phase-encoding lines are acquired per cardiac cycle, an interleaved flow encoding will keep the consecutive samples separated by at least four TRs, in cases of three-directional measurements. Although time-resolved PC-MRI can also be applied to steady in vitro flow, this is usually not done. In such cases, beneficial effects can be obtained by repeating the acquisition multiple times and perform signal averaging. In addition to improving the SNR, this will lead to improved sampling of the turbulence time scales, given that there is a sufficient time difference between the acquisitions of a given phase-encoding line. An alternative, applicable to both in vivo and in vitro studies, is to use an echo planar imaging (EPI) sequence. In this case, the time difference between consecutive phase-encoding lines will be small. However, if compared to a non-EPI sequence, the use of EPI will allow for a large number of signal averages. Ultimately, this could be beneficial in terms of the sampling of the turbulence time scales. It should be noticed that view-to-view variations, such as the ones described here, are a cause of ghosting artifacts, and that ghosting would induce errors in the estimates. An approach which can be used to estimate the effects of ghosting on MR turbulence measurements has been proposed [19] but remains to be validated. However, severe ghosting is normally easily detected in the images.

The spatial acceleration (Fig. 4) in the stenotic part of the flow phantom was as high as 1 m/s over a distance of 2 mm and thus constituted a good test case for assessing the effects of intravoxel mean velocity variations on MR turbulence measurements. Relative to the σ value of interest, defined by $\tilde{\sigma} = 1/k_{\mathrm{v}}$, the maximum contribution from spatial acceleration was less than 3%, in spite of the high acceleration. In the decelerating part of the flow jet, where the elevated values of σ_{IVSD} are located, the contribution was less than 1%. This confirms recent in vivo observations [20] and suggests that the effect of intravoxel mean velocity variations on MR turbulence measurements is negligible.

The results presented in Fig. 6A, B describe the effects of the nonzero mean value of low SNR MR magnitude data. As predicted by theory, the consequence of this for IVSD estimation appears as in Fig. 6C where $k_{\mathrm{v}} \cdot \sigma_{\mathrm{true}}$ values greater than $k_{\mathrm{v}} \cdot \hat{\sigma}$ are underestimated. Note that the value of $k_{\mathrm{v}} \cdot \hat{\sigma}$ in Fig. 6 is dependent on the present noise level. An overall increase in SNR will increase $\hat{\sigma}$ and vice versa.

When scan time is not a critical issue, improved SNR can be obtained by taking the average of repeated measurements of S. Alternatively, each repeated measurement can be carried out with a different k_{v} value. If this is done, it is important to appreciate that low k_{v} values lead to a poor difference in signal magnitude and that high k_{v} values are at risk of being affected by the nonzero mean value of low SNR MR magnitude data (Fig. 6A and B). From our comparison between three approaches that would require the same amount of scan time, it can be seen that a nonweighted least-squares fit of the measurement points is disadvantageous (Fig. 7). Since the best accuracy is obtained when $|S|/|S_0|$ is around 0.6, we have hypothesized here that in applications where multiple k_{v} values are used, a weighted least-squares fit is beneficial. This is confirmed by the results shown in Fig. 7 where the weighted least-squares approach extends the dynamic range (Fig. 7D). An extension of the dynamic range is also obtained by performing signal averaging in IVSD mapping (Fig. 7B). In addition, this approach provides the greatest increase in accuracy at the central part of the dynamic range and should be most beneficial with respect to the sampling of the turbulence time scales. In applications where there is an extremely wide range of σ values of interest, or when an order of magnitude estimation of the σ values cannot be made, the dynamic range extension obtained by the weighted least-squares approach proposed here may be helpful. Optimization of weights was beyond the scope of this work, but it is recommended for application studies. When the σ values of interest can be reasonably approximated, signal averaging using the same k_{v} value is the best option.

6. Conclusion

We have studied the practical consequences of important aspects of the theory underlying MR turbulence measure-ments and presented several findings that may facilitate future applications of the technique. The findings are applicable to all approaches for MR quantification of turbulence that use information contained in the MR signal magnitude. Data acquisition strategies suitable for turbu-lence quantification have been outlined. We have derived an expression that describes the impact of intravoxel mean velocity variations and presented results that suggest that the effects are negligible. We have also investigated the impact of noise. The turbulence estimates may be underestimated if the SNR is low and the k_{v} parameter is set too low in relation to the values of σ being studied. If k_{v} is set too high, the uncertainty in the estimates will increase. The methods for the assessment of the dynamic range presented here can be applied prior to the measurements to design a suitable imaging protocol, as well as retrospectively to evaluate the dynamic range in an acquired dataset. Additionally, we have shown that approaches for MR quantification of turbulence that utilize multiple k_{v} values benefit from using a weighted least-squares approach.

Acknowledgments

References

[1] Sallam AM, Hwang NH. Human red blood cell hemolysis in a turbulent shear flow: contribution of Reynolds shear stresses. Biorheology 1984;21(6):783–97.

[2] Stein PD, Sabbah HN. Measured Turbulence and its effect on thrombus formation. Circ Res 1974;35(4):608–14.

[3] Becker RC, Eisenberg P, Turpie AG. Pathobiologic features and prevention of thrombotic complications associated with prosthetic heart valves: fundamental principles and the contribution of platelets and thrombin. Am Heart J 2001;141(6):1025–37.

[4] Nichols W, O'Rourke M. McDonald's Blood Flow in Arteries. London: Hodder Arnold; 2005.

[5] Malek AM, Alper SL, Izumo S. Hemodynamic shear stress and its role in atherosclerosis. Jama 1999;282(21):2035–42.

[6] Cheng C, Tempel D, van Haperen R, van der Baan A, Groseveld F, Daemen MJAP, et al. Atherosclerotic lesion size and vulnerability are determined by patterns of fluid shear stress. Circulation 2006;113: 2744–53.

[7] Richter Y, Edelman ER. Cardiology is flow. Circulation 2006;113: 2679–82.

[8] Hinze JO. Turbulence. New York: McGraw-Hill; 1975.

[9] Bernard PS, Wallace JM. Turbulent Flow. New Jersey: John Wiley & Sons, Inc; 2002.

[10] Gray RM. Probability, Random Processes, and Ergodic Properties. Berlin: Springer-Verlag; 1988.

[11] de Gennes PG. Theory of spin echoes in a turbulent fluid. Phys Lett 1969;29A(1):20–1.

[12] Nalcioglu O, Cho Z, Xiang Q, Ahn C. Incoherent flow imaging. SPIE 1986;671:285–9.

[13] Kuethe DO. Measuring distributions of diffusivity in turbulent fluids with magnetic-resonance imaging. Phys Rev A 1989;40(8):4542–51.

[14] Gao JH, Gore JC. Turbulent flow effects on NMR imaging: measurement of turbulent intensity. Med Phys 1991;18(5):1045–51.

[15] Gatenby JC, Gore JC. Mapping of turbulent intensity by magnetic resonance imaging. J Magn Reson B 1994;104(2):119–26.

[16] Kuethe DO, Gao JH. NMR signal loss from turbulence: models of time dependence compared with data. Phys Rev E 1995;51(4):3252–62.

[17] Pipe JG. A simple measure of flow disorder and wall shear stress in phase contrast MRI. Magn Reson Med 2003;49(3):543–50.

[18] Dyverfeldt P, Sigfridsson A, Kvitting JPE, Ebbers T. Quantification of intravoxel velocity standard deviation and turbulence intensity by generalizing phase-contrast MRI. Magn Reson Med 2006;56(4):850–8 [Erratum in: Magn Reson Med 2007;57:233].

[19] Elkins CJ, Alley MT, Saetran L, Eaton JK. Three-dimensional magnetic resonance velocimetry measurements of turbulence quantities in complex flow. Exp Fluids 2009;46(2):285–96.

[20] Dyverfeldt P, Kvitting JPE, Sigfridsson A, Engvall J, Bolger AF, Ebbers T. Assessment of fluctuating velocities in disturbed cardiovascular blood flow: in-vivo feasibility of generalized phase-contrast MRI. J Magn Reson Imaging 2008;28(3):655–63.

[21] Elkins CJ, Alley MT. Magnetic resonance velocimetry: applications of magnetic resonance imaging in the measurement of fluid motion. Exp Fluids 2007;43(6):823–58.

[22] Bolger AF, Heiberg E, Karlsson M, Wigström L, Engvall J, Sigfridsson A, et al. Transit of blood flow through the human left ventricle mapped by cardiovascular magnetic resonance. J Cardiovasc Magn Reson 2007;9(5):741–7.

[23] Moran PR. A flow velocity zeugmatographic interlace for NMR imaging in humans. Magn Reson Imaging 1982;1(4):197–203.

[24] Pelc NJ, Bernstein MA, Shimakawa A, Glover GH. Encoding strategies for three-direction phase-contrast MR imaging of flow. J Magn Reson Imaging 1991;1(4):405–13.

[25] Haacke E, Brown R, Thompson M, Venkatesan R. Magnetic Resonance Imaging: Physical Principles and Sequence Design. New York: John Wiley & Sons; 1999.

[26] Stepišnik J, Callaghan P. The long time tail of molecular velocity correlation in a confined fluid: observation by modulated gradient spin-echo NMR. Phys B 2000;292(3-4):296–301.

[27] Sagaut P. Large Eddy Simulation for Incompressible Flows: An Introduction. Berlin: Springer-Verlag; 2002.

[28] Gårdhagen R, Lantz J, Carlsson F, Karlsson M. Large eddy simulation of flow through a stenosed pipe. American Society of Mechanical Engineers Summer Bioengineering Conference, Marco Island, Florida, USA: ASME; 2008.

[29] Romane GP, Ouellette NT, Xu H, Bodenschatz E, Steinberg V, Meneveau C, et al. Measurements of turbulent flow. In: Tropea C, Yarin AL, Foss JF, editors. Handbook of Experimental Fluid Mechanics. Berlin: Springer-Verlag; 2007.

[30] Jones DK, Basser PJ. "Squashing peanuts and smashing pumpkins": how noise distorts diffusion-weighted MR data. Magn Reson Med 2004;52(5):979–93.